

7-27-2015

# Constraining the Redshift Evolution of the Cosmic Microwave Background Blackbody Temperature with *Planck* Data

I. de Martino

*Universidad de Salamanca, Spain*

R. Génova-Santos

*Instituto de Astrofísica de Canarias, Spain*

F. Atrio-Barandela

*Universidad de Salamanca, Spain*

H. Ebeling

*University of Hawaii*

A. Kashlinsky

*NASA Goddard Space Flight Center*

*See next page for additional authors*

**Click here to let us know how access to this document benefits you.**

Follow this and additional works at: [https://uknowledge.uky.edu/physastron\\_facpub](https://uknowledge.uky.edu/physastron_facpub)

 Part of the [Astrophysics and Astronomy Commons](#), and the [Physics Commons](#)

## Repository Citation

de Martino, I.; Génova-Santos, R.; Atrio-Barandela, F.; Ebeling, H.; Kashlinsky, A.; Kocevski, Dale D.; and Martins, C. J. A. P., "Constraining the Redshift Evolution of the Cosmic Microwave Background Blackbody Temperature with *Planck* Data" (2015). *Physics and Astronomy Faculty Publications*. 364.

[https://uknowledge.uky.edu/physastron\\_facpub/364](https://uknowledge.uky.edu/physastron_facpub/364)

This Article is brought to you for free and open access by the Physics and Astronomy at UKnowledge. It has been accepted for inclusion in Physics and Astronomy Faculty Publications by an authorized administrator of UKnowledge. For more information, please contact [UKnowledge@lsv.uky.edu](mailto:UKnowledge@lsv.uky.edu).

---

**Authors**

I. de Martino, R. Génova-Santos, F. Atrio-Barandela, H. Ebeling, A. Kashlinsky, Dale D. Kocevski, and C. J. A. P. Martins

**Constraining the Redshift Evolution of the Cosmic Microwave Background Blackbody Temperature with *Planck* Data****Notes/Citation Information**

Published in *The Astrophysical Journal*, v. 808, no. 2, 128, p. 1-10.

© 2015. The American Astronomical Society. All rights reserved.

The copyright holders have granted the permission for posting the article here.

**Digital Object Identifier (DOI)**

<https://doi.org/10.1088/0004-637X/808/2/128>

# CONSTRAINING THE REDSHIFT EVOLUTION OF THE COSMIC MICROWAVE BACKGROUND BLACKBODY TEMPERATURE WITH *PLANCK* DATA

I. DE MARTINO<sup>1</sup>, R. GÉNOVA-SANTOS<sup>2</sup>, F. ATRIO-BARANDELA<sup>1</sup>, H. EBELING<sup>3</sup>, A. KASHLINSKY<sup>4</sup>, D. KOCEVSKI<sup>5</sup>, AND C. J. A. P. MARTINS<sup>6,7</sup>

<sup>1</sup> Física Teórica, Universidad de Salamanca, E-37008 Salamanca, Spain; [ivan.demartino1983@gmail.com](mailto:ivan.demartino1983@gmail.com), [atrio@usal.es](mailto:atrio@usal.es)

<sup>2</sup> Instituto de Astrofísica de Canarias, E-38200 La Laguna, Spain; [ricardo.genova@iac.es](mailto:ricardo.genova@iac.es)

<sup>3</sup> Institute for Astronomy, University of Hawaii, Honolulu, HI 96822 USA; [ebeling@ifa.hawaii.edu](mailto:ebeling@ifa.hawaii.edu)

<sup>4</sup> NASA Goddard Space Flight Center and SSAI, Observational Cosmology Lab, Greenbelt, MD 20771 USA; [Alexander.Kashlinsky@nasa.gov](mailto:Alexander.Kashlinsky@nasa.gov)

<sup>5</sup> Chemistry-Physics Building, University of Kentucky, Lexington, KY 40508 USA; [kocevski@pa.uky.edu](mailto:kocevski@pa.uky.edu)

<sup>6</sup> Centro de Astrofísica da Universidade do Porto, Rua das Estrelas, 4150-762 Porto, Portugal; [Carlos.Martins@astro.up.pt](mailto:Carlos.Martins@astro.up.pt)

<sup>7</sup> Instituto de Astrofísica e Ciências do Espaço, CAUP, Rua das Estrelas, 4150-762 Porto, Portugal

Received 2015 February 2; accepted 2015 June 3; published 2015 July 27

## ABSTRACT

We constrain the deviation of adiabatic evolution of the universe using the data on the cosmic microwave background (CMB) temperature anisotropies measured by the *Planck* satellite and a sample of 481 X-ray selected clusters with spectroscopically measured redshifts. To avoid antenna beam effects, we bring all of the maps to the same resolution. We use a CMB template to subtract the cosmological signal while preserving the Thermal Sunyaev–Zeldovich (TSZ) anisotropies; next, we remove galactic foreground emissions around each cluster and we mask out all known point sources. If the CMB blackbody temperature scales with redshift as  $T(z) = T_0(1+z)^{1-\alpha}$ , we constrain deviations of adiabatic evolution to be  $\alpha = -0.007 \pm 0.013$ , consistent with the temperature-redshift relation of the standard cosmological model. This result could suffer from a potential bias  $\delta\alpha$  associated with the CMB template. We quantify it to be  $|\delta\alpha| \leq 0.02$ , with the same sign as the measured value of  $\alpha$ . Our result is free from those biases associated with using TSZ selected clusters; it represents the best constraint to date of the temperature-redshift relation of the Big Bang model using only CMB data, confirming previous results.

**Key words:** cosmic background radiation – cosmology: observations – cosmology: theory

## 1. INTRODUCTION

Adiabatic expansion and photon number conservation have produced a cosmic microwave background (CMB) with a blackbody temperature of  $T_0 = 2.725 \pm 0.002$  K (Fixsen 2009) that evolves with redshift  $z$  as  $T(z) = T_0(1+z)$ . This temperature-redshift relation is an important test of the Big Bang paradigm (Avgoustidis et al. 2012) and of spatial homogeneity (Clarkson 2012). Models like decaying vacuum energy density and gravitational “adiabatic” photon creation predict a more general scaling (Overduin & Cooperstock 1998; Matyjasek 1995; Puy 2004; Jetzer et al. 2011). An imprint on the  $T(z)$  relation can be produced if the period of accelerated expansion is driven by a phase transition (Mortonson et al. 2009; Nunes et al. 2009). The nonconservation of the photon number density changes the temperature-redshift and the distance duality relations. Two functional forms have been considered in the literature:  $T(z) = T_0(1+z)^{1-\alpha}$  (Lima et al. 2000) and  $T(z) = T_0(1+bz)$  (LoSecco et al. 2001), with  $\alpha$  and  $b$  constant parameters. At low redshifts, the differences between both functional forms are small and only the first scaling is usually tested. In most scenarios, deviations of adiabatic evolution are associated with distortions of the CMB blackbody spectrum (Chluba 2014) and are strongly constrained by the current FIRAS upper limit of Fixsen (2009). A departure of the standard temperature-redshift relation would represent an important challenge to the current cosmological model and it represents a test of these alternative scenarios.

The earliest measurements on CMB blackbody temperature evolution were obtained using the relative populations of atomic fine-structure levels which are excited by the

background radiation (Songaila et al. 1994; Srianand et al. 2000). Noterdaeme et al. (2010) measured  $T(z = 2.69) = 10.5_{-0.6}^{+0.8}$  K using the rotational excitation of CO molecules in quasar spectral lines, a value compatible with 10.06 K, the blackbody temperature expected at that redshift with the standard temperature-redshift relation. Using quasar spectral lines, the best constraint on deviations from adiabatic evolution at present is  $\alpha = 0.009 \pm 0.019$  (Muller et al. 2013); they also obtained a very stringent individual measurement of the CMB temperature:  $T(z = 0.89) = 5.08 \pm 0.10$  K. Recently, the Planck Collaboration obtained a much tighter constraint (Planck Collaboration 2015) by including data on large-scale structures with the CMB data, but their measurement  $\alpha = (0.2 \pm 1.1) \times 10^{-3}$  applies to models where the deviation from adiabatic evolution starts at the last scattering surface. The temperature-redshift relation has also been probed using the Thermal Sunyaev–Zeldovich effect (Sunyaev & Zeldovich 1970; hereafter TSZ). The TSZ anisotropy induced by clusters of galaxies along the line of sight  $\hat{n}$  is  $\Delta T(\hat{n}) = T_0 G(x) Y_c$ . The Comptonization parameter is defined as  $Y_c = (k_B/m_e c^2) \int T_e d\tau$ , where  $d\tau = \sigma_T n_e dl$  is the cluster optical depth,  $n_e$  and  $T_e$  are the electron density and temperature evaluated along the line of sight  $l$ ,  $\sigma_T$  is the Thomson cross section,  $k_B$  is the Boltzmann constant,  $m_e$  is the electron mass, and  $c$  is the speed of light. This effect depends on the frequency of observation  $\nu_0$  as  $x = h\nu_0(1+z)/k_B T$ , where  $h$  is the Planck constant and  $T = T(z)$  is the CMB blackbody temperature at the cluster location. In the non-relativistic limit,  $G(x) = x \coth(x/2) - 4$ . This spectral dependence is different from that of all known foregrounds, making the TSZ effect an effective tool for detecting clusters as well as

a potential probe of the redshift evolution of the background temperature.

If the universe evolves adiabatically, then  $x$  is independent of redshift. We will test deviations from adiabatic evolution assuming the Lima et al. (2000) parameterization, that is,  $x = h\nu_0(1+z)^\alpha/k_B T_0$  and  $G = G(\nu, \alpha)$ . Fabbri et al. (1978) proposed constraining  $\alpha$  by measuring the zero cross frequency of clusters at different redshifts that, for adiabatic evolution, occurs at  $\nu \simeq 217$  GHz. The measurement of the cross-over frequency is problematic since the TSZ is inherently weak and could be dominated by uncertain systematics. As an alternative, early studies fit the TSZ signal at different frequencies to measure the function  $G(\nu, \alpha)$ . We shall denote this procedure as the fit method. Rephaeli (1980) suggested the ratio method, constraining  $\alpha$  by using the ratio of the TSZ anisotropy at different frequencies,  $R(\nu_1, \nu_2, \alpha) = G(\nu_1, \alpha)/G(\nu_2, \alpha)$ . By taking ratios, the dependence on the Comptonization parameter is removed and there is no need to account for model uncertainties on the gas density and temperature profiles. On the negative side, the analysis is more complicated since the distribution of the temperature anisotropy ratios is highly nonGaussian (Luzzi et al. 2009) and the Kinematic Sunyaev–Zeldovich (Sunyaev & Zeldovich 1972; hereafter KSZ) generated by cluster peculiar velocities is a component that is always present at the cluster location and cannot be separated from the cosmological signal. For a small number of clusters, the effect needs to be taken into account while it is expected to be less important for large cluster samples. Battistelli et al. (2002) found  $\alpha = -0.16^{+0.34}_{-0.32}$  from the TSZ measurement of the Coma and A2163 clusters. Later, from the data on just 13 clusters, Luzzi et al. (2009) set an upper limit of  $\alpha \leq 0.079$  in the range  $z = 0.023$ – $0.546$  at the 68% confidence level.

In 2013, the Planck Collaboration released their first maps of the temperature fluctuations of the CMB sky using 15.5 months of data (Planck Collaboration 2014a). The Low Frequency Instrument (LFI) produced three maps with frequencies of 30, 44, and 70 GHz and angular resolution from 33 to 13'. The High Frequency Instrument (HFI) was sensitive to a wider range of frequencies, from 100 to 857 GHz and scanned the CMB sky at much higher angular resolution, from 10' to 5'. Due to its large frequency coverage, high resolution, and low noise, the *Planck* satellite is an optimal instrument for detecting the TSZ distortion of the CMB spectrum induced by clusters. To clean the CMB data from foreground contributions, the Planck Collaboration also released maps of (a) thermal dust and residual Cosmic Infrared Background emission, (b) synchrotron, free–free and spinning dust emission, (c) CO contributions, which are most important at 100, 217, and 353 GHz, and (d) maps of dust temperature and opacity (Planck Collaboration 2014c). Additional products required to analyze the data, such as masks and noise maps, were also released. Using *Planck* data and a sample of 813 clusters up to redshift  $z \sim 1$ , Hurier et al. (2014) obtained  $\alpha = 0.009 \pm 0.017$ . Their sample included X-ray- and TSZ-selected clusters. Using clusters detected with the South Pole Telescope, Saro et al. (2014) measured  $\alpha = 0.017^{+0.030}_{-0.028}$ , which is also compatible with adiabatic evolution.

In this article, we will apply the techniques developed in de Martino et al. (2012) to test the standard temperature–redshift relation. Our cluster catalog comprises 782 clusters selected from the X-ray *ROSAT* data and with well-measured properties; of those, 481 will be used in this study. The outline of this

paper is as follows. In Section 2, we describe our data and pipeline, in Section 3, we present our results, and in Section 4, we summarize our main conclusions.

## 2. DATA AND DATA PROCESSING

We constrain the temperature–redshift evolution of the background temperature using a cluster catalog selected from *ROSAT* data and the *Planck* Nominal maps released in 2013.<sup>8</sup> We will only use HFI data, originally released in Healpix format with a resolution of  $N_{\text{side}} = 2048$  (Gorski et al. 2005).

### 2.1. Cluster Sample

Our catalog contains 782 clusters, of which 623 are outside of the Planck PCCS-SZ-Union mask (see below; Planck Collaboration 2014e, 2014f). They have been selected from three X-ray flux limited surveys: the *ROSAT*-ESO Flux Limited X-ray catalog (Böhringer et al. 2004), the extended Brightest Cluster Sample (eBCS, Ebeling et al. 1998, 2002) and the Clusters in the Zone of Avoidance (Ebeling et al. 2002). Details of the combined catalog are given in Kocevski & Ebeling (2006). All clusters have well-measured positions, X-ray fluxes, and luminosities in the [0.1, 2.4] KeV *ROSAT* band, spectroscopic redshifts, and angular extents of the X-ray-emitting region. The catalog also lists the X-ray temperature derived from the  $L_X - T_X$  relation of White et al. (1997) and the core radii  $r_c$  and central electron density  $n_{e,0}$  obtained by fitting a  $\beta = 2/3$  model to the *ROSAT* data. We compute the radius at which the mean overdensity of the cluster is 500 times the critical density,  $r_{500}$ , from the  $r_{500} - L_X$  relation of Böhringer et al. (2007). We define  $M_{500}$  as the mass enclosed within a sphere of radius  $r_{500}$  and the angular size  $\theta_{500} = r_{500}/d_A$ , where  $d_A(z)$  is the diameter angular distance of each cluster in the  $\Lambda$ CDM model. In Figure 1, we present the redshift and mass distribution of the clusters in our catalog.

The clusters in our sample have masses in the interval  $M_{500} = (0.2\text{--}10) \times 10^{14} M_\odot$  and are located at redshifts  $z \leq 0.3$ , which are relatively low compared with other catalogs. The catalog used by Hurier et al. (2014) contains X-ray- and *Planck*-selected clusters. Compared with our catalog, the MCXC sample (Piffaretti et al. 2011) includes clusters from sources that we have not considered such as NORAS (Böhringer et al. 2000), SGP (Crudeace et al. 2002), and NEP (Henry et al. 2006). Furthermore, our catalog does not include clusters from X-ray-pointed surveys, which tend to find mainly low-mass systems, but out to high redshift. For redshifts  $z < 0.3$  and masses  $M_{500} \geq 10^{14} M_\odot$  all of our clusters, except 10, are listed in the MCXC sample. In the same mass and redshift range, the *Planck* SZ catalog contains 555 clusters. Of those, only 239 are at less than 10' away from members of our sample. An important difference in the latter catalog is that the Planck Collaboration estimates  $M_{500}$ , using the scaling relation  $M_{500} - Y_{X,500}$  of Arnaud et al. (2010), while we use the  $r_{500} - L_X$  relation from Böhringer et al. (2007); the resulting masses differ, on average, by 30%. Saro et al. (2014) used a sample of 158 clusters with redshifts  $z \leq 1.35$ , selected by their TSZ signal. When cluster candidates are identified using CMB data, the adiabatic evolution is assumed, biasing cluster selection toward those candidates that mimic this behavior. The South Pole group verified that this effect was not significant.

<sup>8</sup> *Planck* data can be downloaded from <http://www.cosmos.esa.int/web/planck>.

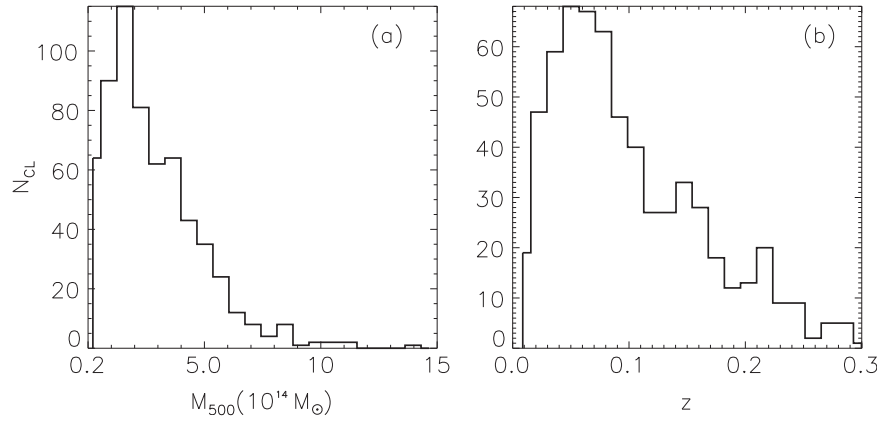


**Figure 1.** Histograms with the mass (a) and redshift (b) distributions of the 481 clusters used in this study.

**Table 1**  
Average Properties of Different Cluster Subsamples from the General Catalog

Subset	N <sub>cl</sub>	$\bar{z}$	$\bar{\theta}_{500}$ (arcmin)	$\bar{L}_X$ ( $10^{44}$ erg s $^{-1}$ )	$\bar{M}_{500}$ ( $10^{14} M_{\odot}$ )
All Clusters	481	0.106	12.3	2.35	3.1
$0.0 < z < 0.05$	32	0.035	21.2	0.51	1.2
$0.05 < z < 0.10$	186	0.074	12.5	1.34	2.4
$0.10 < z < 0.15$	114	0.123	8.82	2.20	3.3
$0.15 < z < 0.20$	83	0.169	7.64	4.17	4.8
$0.20 < z < 0.25$	46	0.222	6.58	6.13	5.8
$0.25 < z < 0.30$	20	0.274	6.15	10.1	7.6
$M_{500} \geq 2 \times 10^{14} M_{\odot}$	397	0.134	10.49	3.40	4.1
$0.0 < z < 0.05$	20	0.039	26.5	1.67	3.1
$0.05 < z < 0.10$	121	0.078	13.4	2.01	3.2
$0.10 < z < 0.15$	107	0.124	8.85	2.28	3.4
$L_X \geq 2.5 \times 10^{44}$ erg s $^{-1}$	201	0.152	13.51	5.32	5.7
$0.0 < z < 0.05$	3	0.037	38.4	3.47	5.2
$0.05 < z < 0.10$	25	0.077	16.6	4.28	5.6
$0.10 < z < 0.15$	36	0.129	9.59	3.51	4.6
$0.15 < z < 0.20$	71	0.171	7.72	4.51	5.1

**Note.** Clusters have been selected by luminosity and mass within each redshift bin.

Nevertheless, due to their selection criteria, negative temperature fluctuations were more likely to be negative than positive, and taking into account this second effect, increased their error bars by 30% (Saro et al. 2014). Therefore, it is important to verify the results of other groups using only X-ray-selected clusters since they will not be affected by these biases. In Table 1, we present the mean redshift, angular scale, X-ray luminosity, and mass averaged over the full cluster sample and, in several subsamples, selected according to X-ray luminosity mass and redshift. For a better comparison, we chose the same redshift bins as those in Hurier et al. (2014); within each redshift bin, we select all clusters with  $M_{500} \geq 2 \times 10^{14} M_{\odot}$  or  $L_X \geq 2.5 \times 10^{44}$  erg s $^{-1}$ . In the table, we do not quote a redshift bin in the mass and X-ray luminosity subsamples when it coincides with the bin of the full sample.

## 2.2. Foreground Cleaned Planck Nominal Maps

The nine frequency maps released by the Planck Collaboration in 2013 contained foreground emissions in addition to the

intrinsic CMB temperature anisotropies and the instrumental noise. Since the different frequencies have different angular resolutions, we bring all of the maps to a common resolution of  $10'$ , the lowest of the HFI channels. Due to their lower resolution and higher instrumental noise, we will not use the LFI data. We remove the cosmological and KSZ anisotropies by subtracting the LGMCA CMB map from Bobin et al. (2013a, 2013b), smoothed to the same  $10'$  resolution. This map was constructed from the latest *Wilkinson Microwave Anisotropy Probe* nine-year and first *Planck* 2013 data releases. The data were combined using a component separation method based on the sparsity of the foregrounds in the wavelet domain that requires frequency information to remove the TSZ effect. The resulting map has low dust contamination at  $\ell < 1000$  and the KSZ anisotropy is preserved while the TSZ signal is removed. In this respect, it is more useful than the *Planck* reconstructions of the CMB anisotropies, like SMICA, that contain substantial TSZ residuals. Next, we clean the foreground emission around each cluster. At frequencies higher than 100 GHz, thermal



dust emission dominates over most of the sky (Planck Collaboration 2014c). This contribution is commonly described as a modified blackbody spectrum with a power-law emissivity  $\epsilon_\nu \propto \nu^{\beta_d}$  with a slope  $\beta_d \approx 1.5\text{--}1.8$  (Planck Collaboration 2014b), independent of frequency but varying across the sky even on scales as small as  $5'$ . The dust contribution is largest at 857 GHz and dominates over the cosmological signal. Then we can use this channel as a template for thermal dust to clean patches  $P(\nu, \mathbf{x})$  centered on each cluster position  $\mathbf{x}$  and on each map of frequency  $\nu$ . When the dust emission parameters and frequency dependence are known, one can generate dust templates at different frequencies to be subtracted from the data. In this paper, we will use a different approach, proposed by Diego et al. (2002), that minimizes the contribution to the map at frequency  $\nu$  of all the foregrounds that correlate with the 857 GHz channel. Specifically, the weight  $w(\nu)$  minimizes the difference  $[P(\nu, \mathbf{x}) - w(\nu)P(857 \text{ GHz}, \mathbf{x})]^2$ . Weights are computed on a ring around the cluster region, defined as  $R = [\theta_{\text{cl}}, \theta_{\text{patch}}]$ , and are given by

$$w(\nu) = \frac{\sum_{\mathbf{x} \in R} P(\nu, \mathbf{x})P(857 \text{ GHz}, \mathbf{x})}{\sum_{\mathbf{x} \in R} [P(857 \text{ GHz}, \mathbf{x})]^2}. \quad (1)$$

To avoid overlapping with the TSZ emission from the clusters in our catalog, we masked a region of  $3\theta_{500}$  around them. Excising these pixels changes the weight by less than 2%. We assume that the dust temperature and spectral index are constant within the ring. This approximation is more accurate for the less extended clusters. Ring sizes vary depending on the cluster extent:  $\theta_{\text{cl}} = 2\theta_{500}$ ,  $\theta_{\text{patch}} = 3\theta_{500}$  for all clusters with  $\theta_{500} \geq 20'$ , otherwise  $\theta_{\text{cl}} = 3\theta_{500}$  and  $\theta_{\text{patch}} = [5\text{--}7]\theta_{500}$ . If we used a ring of the same size for all clusters, the patch would be too large for the most extended clusters and the approximation of constant temperature and constant spectral index would not hold. On the contrary, if  $\theta_{500}$  is too small, then the patch would contain a few pixels and the statistical weight would be unreliable. We checked that the above angular extents yield the smallest foreground residuals around clusters. The procedure is robust since weights did not change if  $\theta_{\text{patch}}$  and  $\theta_{\text{cl}}$  varied by a factor of two. Then, even if the smallest/largest annuli could contain a small TSZ contribution from the cluster or nearby clusters, the weights were not affected.

The first three CO rotational transition lines  $J = 1 \rightarrow 0$ ,  $J = 2 \rightarrow 1$ , and  $J = 3 \rightarrow 2$  at 115, 231, and 346 GHz, respectively, present the largest transmission coefficients making them a significant foreground component in the *Planck* intensity maps. We corrected this contribution using the estimated CO emission maps provided by the Planck Collaboration. Three types of CO maps have been made available (Planck Collaboration 2014d): Type 1 maps are available for the three frequencies, but are too noisy and are sensitive only to the brightest regions on the galactic plane to be useful. Type 2 maps are less noisy, but they are only available at 100 and 217 GHz. We corrected these two frequencies and found the correction to affect the final cleaned patches very little. Since the transition at 353 GHz is the weakest of the three, we expect that the CO contamination at 353 GHz will not produce a significant effect on the final results.

To reduce the contamination from point sources and foreground residuals near the galactic plane, we used the PCCS-SZ-Union mask (Planck Collaboration 2014e, 2014f). This mask was constructed using the *Planck* Catalog of Compact Sources (PCCS). It is the union of six masks, one for each HFI channel, and the mask of the Galactic Plane and the Magellanic Clouds. Our cleaning method does not give satisfactory results for the faintest clusters, so we restricted our analysis to those clusters with a X-ray luminosity in the *ROSAT* [0.1–2.4] KeV band of  $L_X \geq 0.5 \times 10^{44} \text{ erg s}^{-1}$ , reducing the total number of clusters to 481.

To illustrate how effectively our pipeline removes foregrounds and the differences in the final results between low and extended and high and compact redshift clusters, in Figure 2, we show the temperature fluctuation on patches of angular size  $75' \times 75'$  for two clusters: Coma, with an angular extent of  $\theta_{500} = 48.1$  and redshift  $z = 0.023$ , and PSZ1 G355.07+46.20 with  $\theta_{500} = 9.2$  and  $z = 0.21$ . The first and third rows correspond to the temperature anisotropies on the original *Planck* Nominal maps at frequencies of 100–545 GHz. The second and fourth rows show the same regions on the foreground cleaned maps. In Coma and PSZ1 G355.07+46.20, we fixed the temperature range to be  $[-300, 300] \mu\text{K}$  and  $[-200, 200] \mu\text{K}$ , respectively. In the *Planck* Nominal maps, the two circles have angular radii of  $\theta_{\text{cl}}$  (inner circle) and  $\theta_{\text{patch}}$  (outer circle). In the foreground clean maps, the radius corresponds to  $\theta_{500}$ . The TSZ temperature anisotropy is negative at 100 and 143 GHz; at 217 GHz, it is greatly reduced and it changes sign at higher frequencies. The data at 545 GHz is dominated by foreground residuals and our pipeline produces reliable estimates of the TSZ signal only for the brightest clusters. At this frequency, foreground residuals dominate over cluster anisotropies and we could not use it to determine/constrain deviations from adiabatic evolution.

### 2.3. Testing our Cleaning Procedure

We checked that the LGMCA map does not contain significant TSZ residuals by computing the mean temperature anisotropy at the position of our clusters on disks of different sizes, in units of  $\theta_{500}$ . In Figure 3(a), blue squares and red solid circles represent the mean at the actual position of our 481 clusters and the mean at 481 random positions in the sky, respectively. The error bars are the error on the mean estimated from 100 simulations. For a better view, the results are displayed slightly shifted. The averages at the cluster positions are marginally biased toward negative values compared with a random distribution. For apertures  $\geq \theta_{500}$ , this bias is  $\sim -1 \mu\text{K}$  or smaller and well within the error bar. Since the TSZ is removed from the LGMCA map using the standard ( $\alpha = 0$ ) frequency dependence of the effect, this offset could be systematic and not the mean of some random residuals left at the cluster locations by the component separation process. If  $\alpha \neq 0$ , the TSZ residuals that would remain would change with frequency. If the offset were systematic, the TSZ effect would be shifted upward by  $1 \mu\text{K}$  after subtracting the LGMCA map, modifying the dependence with  $\alpha$ , but not removing it. We will discuss this point further in Section 3.3.

To illustrate that the TSZ anisotropy has been preserved in our foreground cleaned and CMB subtracted maps, in Figure 3(b), we plot the mean temperature anisotropy averaged on a disk of radius  $\theta_{500}$ . Open triangles correspond to the profile of the Coma cluster, while solid circles correspond to PSZ1

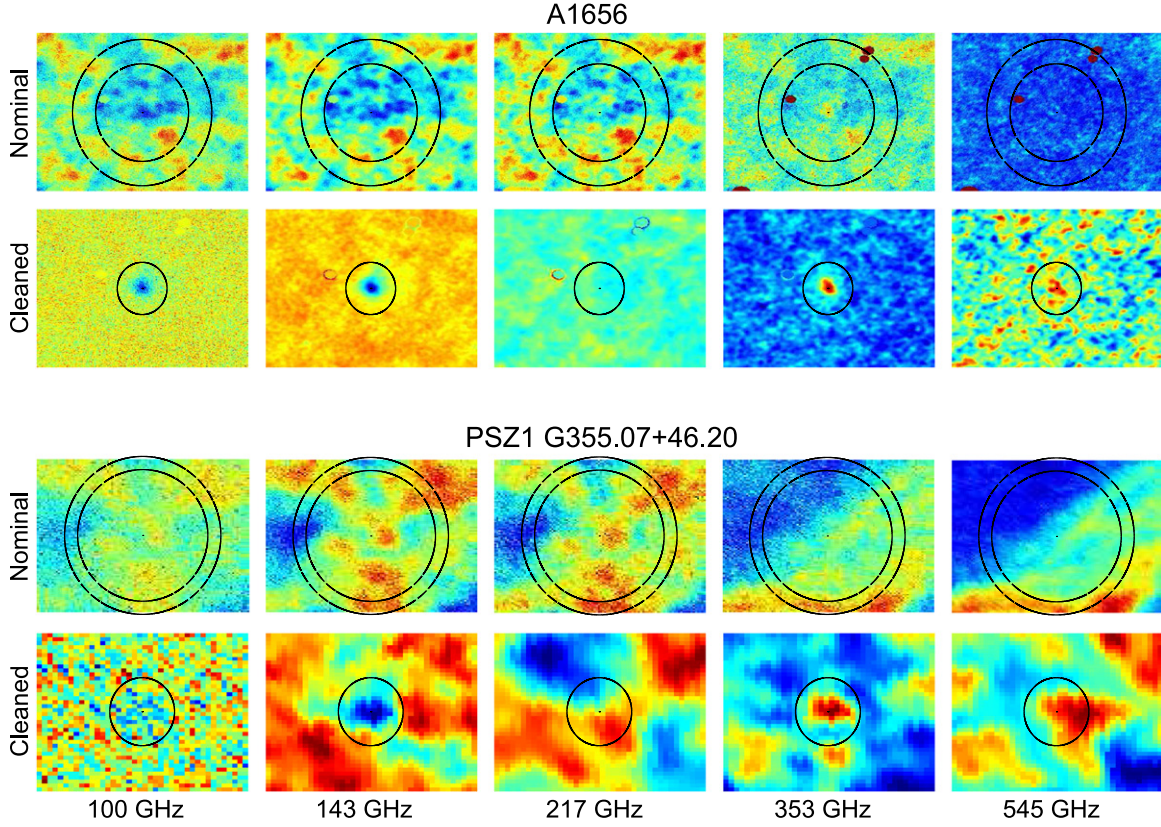


**Figure 2.** Original *Planck* nominal and foreground cleaned patches centered on the position of the Coma [A1656] and the PSZ1 G355.07+46.20 clusters at the HFI frequencies 100–545 GHz. Blue/red colors correspond to negative/positive temperature fluctuations. For Coma, the patch is  $7^\circ \times 7^\circ$  in size and the temperature range is  $[-300, 300] \mu\text{K}$ ; for PSZ1 G355.07+46.20 the size of the patch is  $2.5 \times 2.5$  in the nominal and  $1^\circ \times 1^\circ$  in the cleaned maps and the temperature is within  $[-200, 200] \mu\text{K}$ . In the nominal maps, the inner and outer circles have radii  $\theta_{\text{cl}}$  and  $\theta_{\text{patch}}$ , respectively; in the cleaned maps, the angular radius is  $\theta_{500}$  for the given cluster.

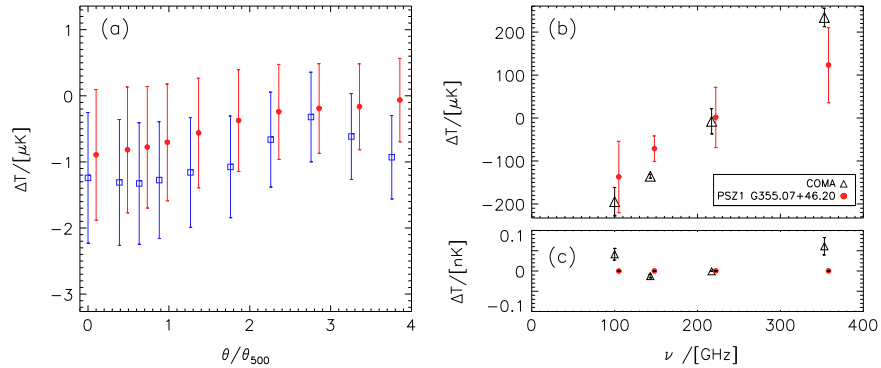


**Figure 3.** (a) Mean temperature anisotropy and its error evaluated on the LGMCA map on disks of different radius, in units of the  $\theta_{500}$ . Blue open squares and red solid circles correspond to the average at the real position of the 481 real clusters and at the same number of random locations on the sky, respectively. The error bars represent the error on the mean. (b) TSZ anisotropy, measured on a disk of size  $\theta_{500}$  on our CMB, removed foreground cleaned data as a function of frequency for the two clusters represented in Figure 2. Red circles have been shifted in order to facilitate their view. (c) Average temperature anisotropy evaluated in the ring  $[\theta_{\text{cl}}, \theta_{\text{patch}}]$  for the same two clusters. The error for PSZ1 G355.07+46.20 is too small to be seen in the figure.

G355.07+46.20. The error bars were computed by placing disks with the same angular extent at one thousand random positions outside of the clusters in our sample; they are much smaller than those of Figure 3(a) since only the instrumental noise and foreground residuals contribute. The difference in the errors between both clusters are due to their different angular extent. Third, we verified that there are no TSZ anisotropy on the rings selected to compute the weights of Equation (1) that could potentially bias the result. Figure 3(c) shows that the mean temperature anisotropy on the rings around of the two clusters is  $\sim 10^{-4} \mu\text{K}$ , negligible compared with the errors on the

cluster profiles; around other clusters, the mean was always  $\leq 10^{-3} \mu\text{K}$ , which is also negligible. To conclude, subtracting the LGMCA map from *Planck* Nominal maps effectively removes the cosmological CMB and KSZ signals while preserving the TSZ anisotropy and its dependence on  $\alpha$ .

#### 2.4. Error Bar Estimation

For each cluster configuration, error bars were computed by evaluating the mean temperature fluctuation on 1000 random positions in foreground cleaned maps on a disk with the same angular extent as the clusters in any given subsample. The

random positions were chosen to be at least  $2^\circ$  away from the location of our clusters to guarantee that the random disks will never overlap with them. We removed the foreground contamination using the same procedure as at cluster locations. We verified that the mean of the simulations was compatible with zero. The correlation matrix between different frequencies was computed by averaging over all simulations:

$$C(\nu_i, \nu_j) = \frac{\langle [\delta T(\nu_i) - \mu(\nu_i)][\delta T(\nu_j) - \mu(\nu_j)] \rangle}{\sigma(\nu_i)\sigma(\nu_j)}, \quad (2)$$

where  $\mu(\nu_i) = \langle \delta T(\nu_i) \rangle$ , and  $\sigma(\nu_i) = \langle [\delta T(\nu_i) - \mu(\nu_i)]^2 \rangle^{1/2}$ . To compare with previous work, we repeated the process and computed the correlation matrix between foreground cleaned maps before subtracting the LGMCA map using our full catalog and compared it with the correlation matrix of Hurier et al. (2014), obtained with a different cluster catalog. While the latter authors used a fixed aperture of  $20'$ , for all clusters, we chose apertures of size  $\theta_{500}$  for each cluster. We found that our off-diagonal terms were slightly smaller; the difference between the two correlation matrices differed between 2% for the element  $C(100, 143 \text{ GHz})$  to less than 10% for  $C(100, 353 \text{ GHz})$ , allowing us to conclude that our cleaning procedure was comparatively as effective as theirs.

### 3. RESULTS

To estimate/constrain the temperature-redshift relation we used the ratio and fit methods described in the Introduction. We derived an X-ray temperature for all clusters in our catalog from the measured X-ray luminosity using the  $L_X$ - $T_X$  relation of White et al. (1997). The cluster temperature allowed us to include relativistic corrections (Itoh et al. 1998; Nozawa et al. 2006). If we denote  $\theta_e = (k_B T_e / m_e c^2)$ , the frequency dependence of the TSZ effect including relativistic corrections up to the fourth order in the cluster temperature,  $G_4(\nu)$ , can be written as

$$G_4(\nu) = G(\nu) \left[ 1 + \theta_e \left( \frac{Y_1}{Y_0} \right) + \theta_e^2 \left( \frac{Y_2}{Y_0} \right)^2 + \theta_e^3 \left( \frac{Y_3}{Y_0} \right)^3 + \theta_e^4 \left( \frac{Y_4}{Y_0} \right)^4 \right], \quad (3)$$

where  $Y_0, \dots, Y_4$  are defined in Equations (2.24)–(2.29) of Nozawa et al. (1998). The correction is relatively small; for the most massive clusters, it amounts to a few percent. Corrections depending on the unknown cluster peculiar velocities were not included, but for the values expected in the concordance model, they are also negligible. Hereafter, in order to simplify the notation, we will drop the subindex; it should be understood that relativistic corrections were included except when indicated otherwise. Finally, let us mention that as a prior we considered  $\alpha = [-1, 1]$ , subdivided in 2001 equally spaced steps.

#### 3.1. Ratio Method

As indicated in Section 2.2, all maps were reduced to a common resolution of  $10'$  to eliminate the differences in the angular resolution. In this statistic, the ratio of the mean

temperature anisotropy on a disk of a fixed angular size  $\theta_{cl}$  at two frequencies,  $\overline{\delta T}(\nu_1)/\overline{\delta T}(\nu_2)$ , does not depend on the cluster pressure profile. In the absence of noise, this ratio would be equal to the theoretical value at each redshift  $R(\nu_1, \nu_2, \alpha) = G(\nu_1, \alpha)/G(\nu_2, \alpha)$ , providing a direct measurement of  $\alpha$ . However, instrumental noise and foreground residuals complicate the analysis. As discussed in Luzzi et al. (2009), for each cluster  $j$  the probability distribution of the ratios,  $\mathcal{P}_j(R)$ , is

$$\mathcal{P}_j(R(\nu_1, \nu_2, \alpha)) = \frac{1}{2\pi\sigma_{\nu_1}\sigma_{\nu_2}} \times \int_{-\infty}^{\infty} x \exp \left( - \left[ \frac{x - \overline{\delta T}(\nu_1)}{2\sigma_{\nu_1}} \right]^2 + \frac{[xR(\nu_1, \nu_2, \alpha) - \overline{\delta T}(\nu_2)]^2}{2\sigma_{\nu_2}^2} \right) dx, \quad (4)$$

where  $\sigma_\nu$  is the error on mean temperature at the cluster location  $j$  at frequency  $\nu$ . The likelihood function is  $\mathcal{L} \propto \prod_j \mathcal{P}_j$ ; we did not include the correlation between the different frequencies, thus our analysis will underestimate the errors. We took five ratios between frequencies from 100 to 353 GHz: 100/353, 143/353, 217/353, 100/143, and 217/143. In the denominator, we chose the channel with the smallest instrumental noise and excluded 217 GHz to avoid dividing by zero when  $\alpha \simeq 0$ . Temperature anisotropies were evaluated on disks of radii  $\theta_{cl} = \theta_{500}$ . Following Hurier et al. (2014), we divided our sample into six redshift bins of equal width  $\Delta z = 0.05$ ; therefore, in Equation (4)  $\overline{\delta T}(\nu_1)$  and  $R(\nu_1, \nu_2, \alpha)$  are now the averages over all the clusters in the bin.

In Figure 4, we plot the likelihood function for different cluster subsets: In (a), we considered the 201 most X-ray-luminous clusters, with X-ray luminosity  $L_X \geq 2.5 \times 10^{44} \text{ erg s}^{-1}$ , in (b) the 397 clusters with mass  $M_{500} \geq 2 \times 10^{14} M_\odot$  and, finally, in (c) we plot the likelihood of our full cluster sample. For illustration, only the likelihood of three redshift bins are plotted. In each panel, the dotted, dashed-dotted, and dashed lines correspond to the bins  $[0.05, 0.1]$ ,  $[0.15, 0.2]$ ,  $[0.25, 0.3]$ , respectively, and the solid lines correspond to the full sample. The measured values of  $\alpha$  are given in Table 2; within each redshift bin, we computed  $\alpha$  in different subsamples, with clusters selected in X-ray luminosity and mass as indicated in Table 1 in order to test the relative contribution of the different cluster subsamples to the final error budget. In all redshift bins, the results are always compatible with zero. Notice that our error bars do not necessarily scale with the square root of the number of clusters since, as indicated in Section 2.2, our cleaning procedure, and consequently the amplitude of the foreground residuals, depend on the cluster extent. We checked that the results were very similar if the temperature averages were taken on disks of radii  $\theta_{cl} = 2\theta_{500}$ . Using the full sample, we constrain the deviation from adiabatic invariance to be  $\alpha = -0.03 \pm 0.06$ . This estimate is a factor of two worse than the result obtained by the SPT group (Saro et al. 2014), even with our underestimated error bars. This is to be expected since their maps have a resolution of  $1.5'$  and even if their sample is smaller in size



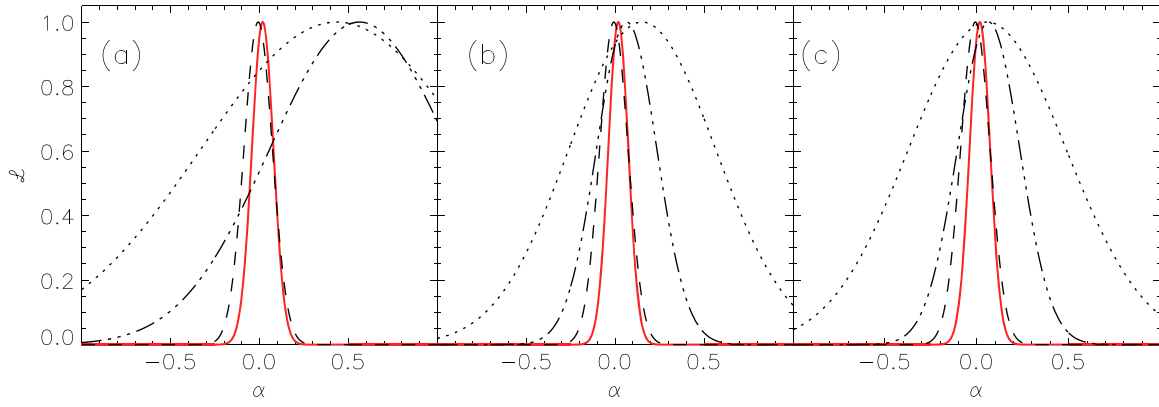


**Figure 4.** Ratio method: (a) likelihoods corresponding to 201 clusters with  $L_X \geq 2.5 \times 10^{44} \text{ erg s}^{-1}$ , in (b) to 397 clusters with  $M_{500} \geq 0.2 \times 10^{15} M_\odot$  and in (c) to the full sample of 481 clusters. Dotted, dashed-dotted, and dashed lines correspond to clusters in the interval  $z = [0.05, 0.1]$ ,  $z = [0.15, 0.2]$ , and  $[0.25, 0.3]$ , respectively. The red solid lines correspond to the full likelihood. Anisotropies were taken as averages on disks of size  $\theta_{500}$ .

**Table 2**  
Values of  $\alpha$ , Estimated Using the Ratio Method

Subset	$N_{\text{cl}}$	$\alpha_{L_X}$	$\sigma_{\alpha_{L_X}}$	$N_{\text{cl}}$	$\alpha_{M_{500}}$	$\sigma_{\alpha_{M_{500}}}$	$N_{\text{cl}}$	$\alpha_{\theta_{500}}$	$\sigma_{\alpha_{\theta_{500}}}$
All	201	0.02	0.06	397	0.02	0.06	481	0.02	0.06
$0.0 < z < 0.05$	3	0.13	1.0	20	-0.05	0.74	32	0.03	0.67
$0.05 < z < 0.10$	25	0.44	0.77	121	0.15	0.41	186	0.06	0.43
$0.10 < z < 0.15$	36	0.95	1.27	107	0.32	0.34	114	0.26	0.29
$0.15 < z < 0.20$	71	0.56	0.51	83	0.07	0.17	83	0.07	0.17
$0.20 < z < 0.25$	46	0.01	0.01	46	0.01	0.01	46	0.01	0.01
$0.25 < z < 0.30$	20	-0.01	0.08	20	-0.01	0.08	20	-0.01	0.08

**Note.** Temperatures are averaged on disks of radius  $\theta_{500}$  over all the clusters in the redshift bin.

their clusters are, on average, at higher redshifts where the effect of the nonadiabatic evolution is most noticeable.

### 3.2. Frequency Fit Method

As an alternative method, we constrain the adiabatic evolution of the universe by fitting the frequency dependence of the TSZ anisotropy,  $\Delta T(\hat{n}) = T_0 \bar{Y}_C G(\nu, \alpha)$ . The Comptonization parameter  $\bar{Y}_C$  is the average on a disk of radius  $\theta_{500}$ . We follow Hurier et al. (2014) and take it as a free parameter. In this case, both  $\bar{Y}_C$  and  $\alpha$  are fit to the data. We took the flat prior  $\bar{Y}_C = [0, 300] \mu\text{K}$  divided in intervals of  $\Delta \bar{Y}_C = 0.15 \mu\text{K}$ . Since all maps have the same resolution,  $\bar{Y}_C$  is independent of frequency. We compute the likelihood function as

$$-2 \log \mathcal{L} = \sum_{i,j} \sum_{k=1}^{N_{\text{cl}}} [\delta \bar{T}_k(\nu_i) - \bar{Y}_{C,k} G(\nu_i, \alpha)] \times C^{-1}(\nu_i, \nu_j) [\delta \bar{T}_k(\nu_j) - \bar{Y}_{C,k} G(\nu_j, \alpha)], \quad (5)$$

where  $C(\nu_i, \nu_j)$ , given in Equation (2), is

$$C(\nu_i, \nu_j) = \begin{pmatrix} 1.0000 & 0.9258 & 0.4603 & 0.1435 \\ 0.9258 & 1.0000 & 0.4995 & 0.3168 \\ 0.4603 & 0.4995 & 1.0000 & 0.3605 \\ 0.1435 & 0.3168 & 0.3605 & 1.0000 \end{pmatrix}, \quad (6)$$

where  $\nu_i = (100, 143, 217, 353) \text{ GHz}$ . Notice that by using the LGMCA map to subtract the intrinsic CMB signal, we have significantly reduced the correlation between frequencies and the variance of the foreground clean maps compared to Hurier et al. (2014).

In Figure 5, we present the likelihood function, marginalized over the Comptonization parameter, for the same cluster subsamples and redshift bins as in Figure 4, with lines following the same convention. The numerical results are given in Table 3; in this case, we find that  $\alpha = -0.007 \pm 0.013$ , which is compatible with zero. We verified that changing the prior to  $\bar{Y}_C = [-300, 300] \mu\text{K}$ , which would allow for foreground residuals to change the sign of the TSZ effect, did not modify the error bars, indicating that the data prefers negative values in the Rayleigh–Jeans and positive values in the Wien part of the spectrum. To illustrate the accuracy of our results, in Figure 6, we plot the average temperature anisotropies of all the clusters the redshift bins of Table 1 and their errors, for the different frequencies. The solid line corresponds to the best fit  $\bar{Y}_C G(\nu, \alpha)$  without relativistic corrections and the dashed line to the best fit including these corrections. Notice that only at  $z > 0.2$  can this correction be distinguished from the nonrelativistic effect. We also indicate the  $\chi^2$  per degree of freedom of the best-fit model.

Our result represents a 30% improvement over Hurier et al. (2014) and it was obtained with a smaller sample of clusters located at a lower mean redshift. In Figure 7, we present a more thorough comparison. The shaded regions correspond to the 1 and 3 $\sigma$  errors given in Table 3. Notice that in the same redshift range, the measured values are in excellent agreement and are fully compatible with an adiabatic evolution of the universe, the main difference being that our error bars are significantly smaller. The reduction on the uncertainty is due to using an accurate CMB template to subtract the cosmological signal.

We can use the upper limit on  $\alpha$  given above to constrain the phenomenological model of Lima et al. (2000) using the temperature-redshift relation derived by Jetzer et al. (2011).

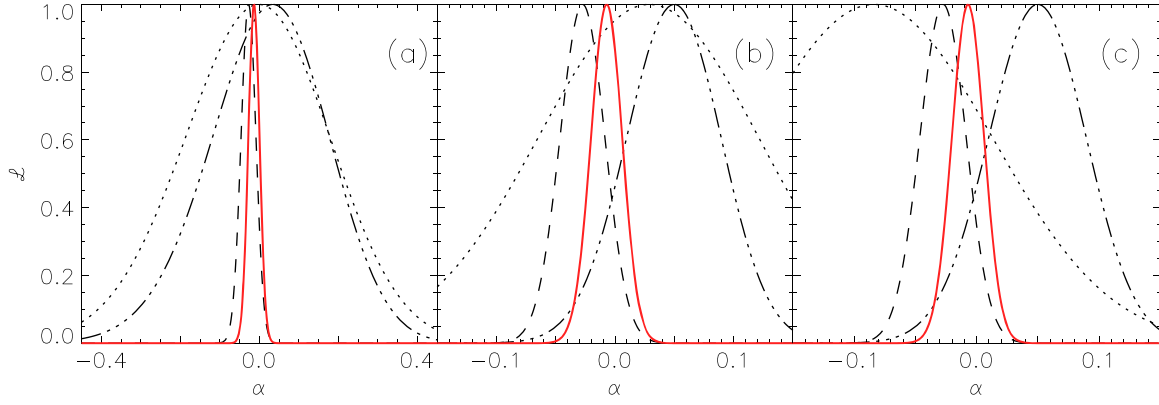


**Figure 5.** Fit method: panels represent the same likelihoods as in Figure 4 and lines follow the same convention.

**Table 3**  
Estimated Values of  $\alpha$  and Their Uncertainties Using the Fit Method

Subset	$N_{\text{cl}}$	$\alpha_{LX}$	$\sigma_{\alpha_{LX}}$	$N_{\text{cl}}$	$\alpha_{M500}$	$\sigma_{\alpha_{M500}}$	$N_{\text{cl}}$	$\alpha_{\theta 500}$	$\sigma_{\alpha_{\theta 500}}$
All	201	-0.013	0.014	397	-0.006	0.013	481	-0.007	0.013
$0.0 < z < 0.05$	3	-0.27	0.23	20	-0.21	0.17	32	-0.16	0.16
$0.05 < z < 0.10$	25	0.00	0.18	121	0.03	0.09	186	-0.08	0.09
$0.10 < z < 0.15$	36	0.08	0.20	107	-0.01	0.09	114	-0.03	0.07
$0.15 < z < 0.20$	71	0.03	0.05	83	0.05	0.04	83	0.05	0.04
$0.20 < z < 0.25$	46	0.01	0.02	46	0.01	0.02	46	0.01	0.02
$0.25 < z < 0.30$	20	-0.03	0.02	20	-0.03	0.02	20	-0.03	0.02

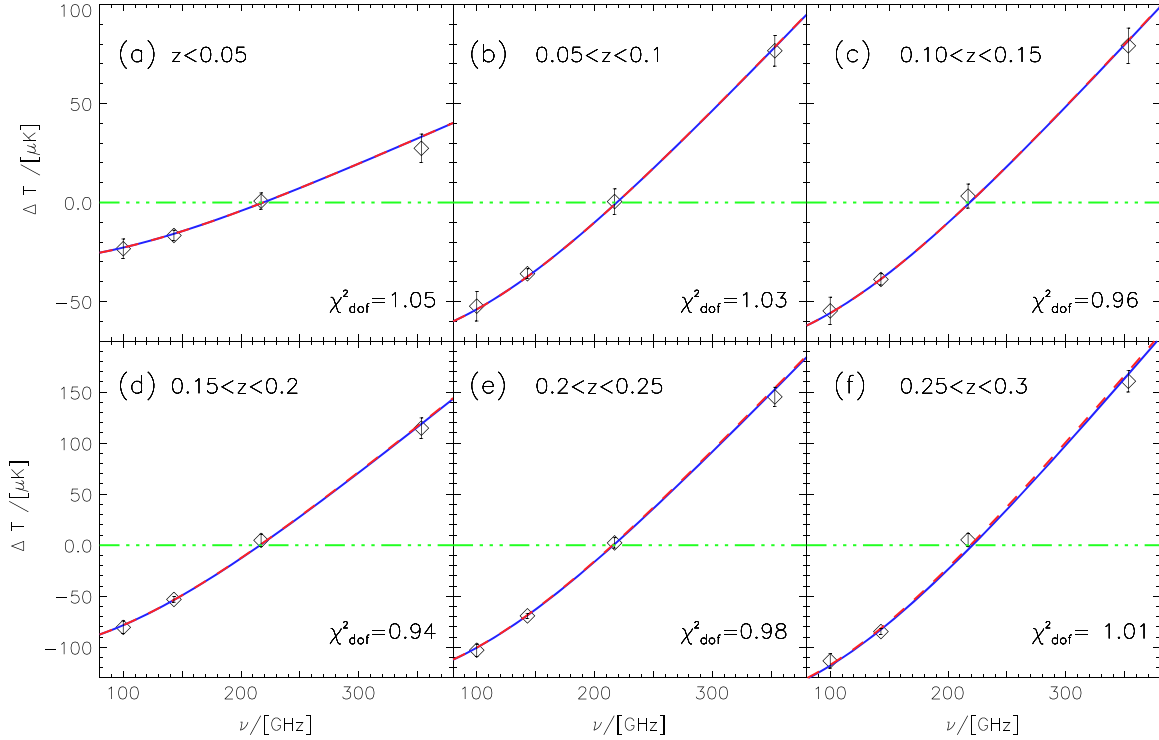


**Figure 6.** Frequency dependence of the TSZ temperature anisotropies averaged over the cluster in the redshift subsamples. Solid lines correspond to the standard adiabatic evolution,  $\alpha = 0$ , without relativistic corrections while dashed lines include these corrections.

The constraint is given in terms of the effective equation of state of a hypothetical decaying dark energy model. From the bounds on the deviation from adiabatic invariance, we find

$w_{\text{eff}} = -1.005 \pm 0.008$ , which is fully compatible with the concordance  $\Lambda$ CDM model. This constraint represents a 20% improvement over the latest measurement of Saro et al. (2014).

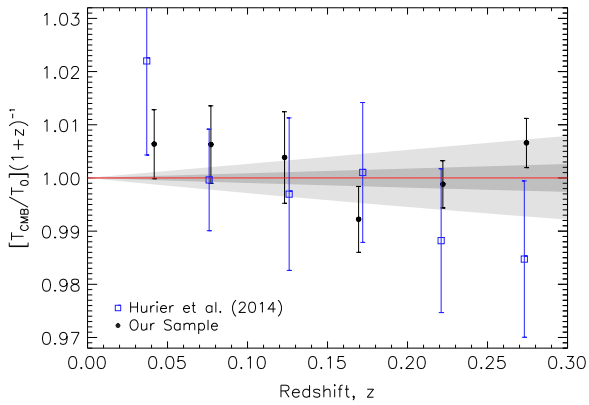


**Figure 7.** Constraints on the adiabatic evolution of the background temperature at different redshifts given in Figure 6. The results of Table 3 are represented by solid circles with their associated error bars. For comparison, open squares and error bars correspond to the results of Hurier et al. (2014). Points are displayed at the mean redshift of the clusters in the bin. The shaded areas correspond to the 68% and 99.7% confidence levels.

### 3.3. Possible Systematic Effects

Our estimates do not take into account the effect of subtracting the TSZ effect from the LGMCA map using the  $G(\nu, \alpha = 0)$  frequency dependence. Figure 3(a) shows that the average temperature anisotropy at the cluster locations has an approximately  $-1 \mu\text{K}$  residual compared to the same measurement at random positions in the sky, averaged over 100 realizations. This difference is well within the errors and compatible with sample variance. We checked that the average of the six redshift bins was random, oscillating around the mean, indicating that there was no such systematic effect. Nevertheless, if the redshift evolution has  $\alpha \neq 0$ , then a residual TSZ would exist at the cluster location and we need to consider the biases introduced if the  $-1 \mu\text{K}$  difference was in fact systematic. Since the LGMCA map is a combination of *WMAP* and *Planck* data at different frequencies, when subtracting the same LGMCA map to all *Planck* Nominal maps, the residual TSZ anisotropy would shift the zero cross frequency but would not change the dependence on  $\alpha$ . The magnitude and sign of the temperature shift are difficult to predict since they would depend on the cluster redshift, mass, and extent and on the LGMCA mixing matrices estimated for a set of input channels on a patch of data at a given wavelet scale. We reanalyzed the data subtracting a fixed  $1 \mu\text{K}$  from the measured temperature anisotropies of all the clusters and at all frequencies and obtained that the value of  $\alpha$  decreased by  $\delta\alpha = -0.02$  in the fit method and remained within the errors in the ratio method; i.e., we would be obtaining a value closer to  $\alpha = 0$  by this amount. If  $\alpha > 0$  then the residual TSZ at the cluster location would be positive, as would be the bias in  $\alpha$ . Therefore, by using the TSZ frequency dependence of an adiabatically evolving universe, our method could be masking the effect of a nonadiabatic evolution. Taking into account this effect, our final constraint would be  $\alpha = -0.007 \pm 0.013$  ( $-0.02$ ) where the parenthesis indicates the systematic contribution. At the  $2\sigma$  level, this result is both compatible with all the upper limits from TSZ and with the spectral lines.

## 4. CONCLUSIONS

We have constrained the deviation of the adiabatic evolution of the CMB blackbody temperature applying two different

estimators to a sample of X-ray-selected clusters and using foreground-cleaned *Planck* Nominal maps. By not including clusters selected by their TSZ signature, we avoid biasing our sample to those clusters that are closest to adiabatic evolution. Following Hurier et al. (2014), we distributed our cluster in six bins of redshift. The constraints on using the ratio and fit methods were  $\alpha = -0.03 \pm 0.06$  and  $\alpha = -0.007 \pm 0.013$ , respectively; the fit method produced statistically more significant results than the ratio method since the latter is very sensitive to small denominators. The constraints are weakened if we add a hypothetical systematic effect due to the component separation method used to construct the LGMCA map and become  $\alpha = -0.007 \pm 0.013$  ( $-0.02$ ) and  $\alpha = -0.03 \pm 0.06$  ( $-0.02$ ), which is compatible with the results given in the literature at the  $2\sigma$  confidence level.

Compared to Saro et al. (2014), the errors in the ratio method are at least a factor of two worse. While our sample contains four times as many clusters, they are located at much lower redshift, where the statistic is less sensitive. However, our implementation of the fit method provides the best constraints on  $\alpha$  to date using only CMB data. For instance, as illustrated in Figure 7, by using the LGMCA reconstruction of the intrinsic CMB temperature anisotropies to remove the cosmological contribution from our maps, we have reduced the errors compared with Hurier et al. (2014) and obtained the best bound to date. The constraint is also interesting since our cluster sample has the lowest mean redshift. We constrain deviations of adiabatic evolution within  $z \leq 0.3$ , well in the period of accelerated expansion. Our results are comparable with a similar analysis carried out by Luzzi et al. (2015), using a catalog of clusters at higher redshifts and fully complements their findings.

Since our clusters have been selected using X-ray data, they are not affected by possible biases associated with selecting clusters using the TSZ effect, providing a consistency check to previous results. We continue to expand our X-ray-cluster sample to probe higher redshifts, where systematic biases would be larger and could be estimated better. Chluba (2014) has argued that low redshift energy injections that could produce a nonadiabatic evolution of the universe are strongly constrained by the upper limit set by FIRAS. Nevertheless, and independently of theoretical expectations, measurements of the temperature-redshift relation of the CMB blackbody temperature provide a strong consistency check of the current Big Bang paradigm.

We thank the referee for his/her comments that helped to improve the manuscript. This work was done in the context of the FCT/MICINN cooperation grant “Cosmology and Fundamental Physics with the Sunyaev–Zel’dovich Effect” AIC10-D-000443, with additional support from projects FIS2012-30926 from the Ministerio de Educación y Ciencia, Spain and PTDC/FIS/111725/2009 from FCT, Portugal. C.M. is also supported by a FCT Research Professorship, contract reference IF/00064/2012, funded by FCT/MCTES (Portugal) and POPH/FSE (EC).

## REFERENCES

- Arnaud, M., Pratt, G. W., Piffaretti, R., et al. 2010, *A&A*, **517**, 92
- Avgoustidis, A., Luzzi, G., Martins, C. J. A. P., & Monteiro, A. M. R. V. L. 2012, *JCAP*, **1202**, 013
- Battistelli, E. S., De Petris, M., Lamagna, L., et al. 2002, *ApJL*, **580**, L101

- Bobin, J., Sureau, F., Starck, J.-L., Rassat, A., & Paykari, P. 2013a, *A&A*, **523**, L4
- Bobin, J., Sureau, F., Paykari, P., et al. 2013b, *A&A*, **533**, 105
- Böhringer, H., Schuecker, P., Pratt, G. W., et al. 2007, *A&A*, **469**, 363
- Böhringer, H., Voges, W., Huchra, J. P., et al. 2000, *ApJS*, **129**, 435
- Chluba, J. 2014, *MNRAS*, **443**, 1881C
- Clarkson, C. 2012, *CRPhy*, **13**, 682
- Crudace, R., Voges, W., Böhringer, H., et al. 2002, *ApJS*, **140**, 239
- de Martino, I., Atrio-Barandela, F., da Silva, A., et al. 2012, *ApJ*, **757**, 144
- Diego, J. M., Vielva, P., Martínez-Gonzalez, E., Silk, J., & Sanz, J. L. 2002, *MNRAS*, **336**, 1351
- Ebeling, H., Edge, A. C., Allen, S. W., et al. 2000, *MNRAS*, **318**, 333
- Ebeling, H., Edge, A. C., Böhringer, H., et al. 1998, *MNRAS*, **301**, 881
- Ebeling, H., Mullis, C. R., & Tully, R. B. 2002, *ApJ*, **580**, 774
- Fabbri, R., Melchiorri, F., & Natale, V. 1978, *Ap&SS*, **59**, 223
- Fixsen, D. J. 2009, *ApJ*, **707**, 916
- Gorski, K., Hivon, E., Banday, A., et al. 2005, *ApJ*, **622**, 759
- Henry, J. P., Mullis, C. R., Voges, W., et al. 2006, *ApJS*, **162**, 304
- Hurier, G., Aghanim, N., Douspis, M., & Pointecouteau, E. 2014, *A&A*, **561**, 143
- Itoh, N., Kohyama, Y., & Nozawa, S. 1998, *ApJ*, **502**, 7
- Jetzer, P., Puy, D., Signore, M., & Tortora, C. 2011, *GReGr*, **43**, 1083
- Kocevski, D. D., & Ebeling, H. 2006, *ApJ*, **645**, 1043
- Lima, J. A. S., Silva, A. I., & Viegas, S. M. 2000, *MNRAS*, **312**, 747
- LoSecco, J. M., Mathews, G. J., & Wang, Y. 2001, *PhRvD*, **64**, 123002
- Luzzi, G., Génova-Santos, R., Martins, C. J. A. P., de Petris, M., & Lamagna, L. 2015, arXiv:1502.07858
- Luzzi, G., Shimon, M., Lamagna, L., et al. 2009, *ApJ*, **705**, 1122
- Matyjasek, J. 1995, *PhRvD*, **51**, 4154
- Mortonson, M., Hu, W., & Huterer, D. 2009, *PhRvD*, **80**, 067301
- Muller, S., Beelen, A., Black, J. H., et al. 2013, *A&A*, **551**, 109
- Noterdaeme, P., Petitjean, P., Srianand, R., Ledoux, C., & López, S. 2010, *MNRAS*, **403**, 906
- Nozawa, S., Itoh, N., & Kohyama, Y. 1998, *ApJ*, **508**, 17
- Nozawa, S., Itoh, N., Suda, Y., & Ohhata, Y. 2006, *Nuovo Cimento*, **121**, 487
- Nunes, N. J., Dent, T., Martins, C. J. A. P., & Robbers, G. 2009, *MmSAI*, **80**, 785
- Overduin, J. M., & Cooperstock, F. I. 1998, *PhRvD*, **58**, 043506
- Piffaretti, R., Arnaud, M., Pratt, G. W., et al. 2011, *A&A*, **534**, 109
- Planck Collaboration 2014a, *A&A*, **571**, 1
- Planck Collaboration 2014b, *A&A*, **571A**, A11
- Planck Collaboration 2014c, *A&A*, **571**, 12
- Planck Collaboration 2014d, *A&A*, **571**, 13
- Planck Collaboration 2014e, *A&A*, **571**, 28
- Planck Collaboration 2014f, *A&A*, **571**, 29
- Planck Collaboration 2015, arXiv:1502.01589
- Puy, D. 2004, *A&A*, **422**, 1
- Rephaeli, Y. 1980, *ApJ*, **241**, 858
- Saro, A., Liu, J., Mohr, J. J., et al. 2014, *MNRAS*, **440**, 2610
- Songaila, A., Cowie, L. L., Hogan, C. J., & Rugers, M. 1994, *Natur*, **368**, 599
- Srianand, R., Petitjean, P., & Ledoux, C. 2000, *Natur*, **408**, 931
- Sunyaev, R. A., & Zeldovich, Y. B. 1970, *Ap&SS*, **7**, 20
- Sunyaev, R. A., & Zeldovich, Y. B. 1972, *CoASP*, **4**, 173
- Sunyaev, R. A., & Zeldovich, Y. B. 1980, *MNRAS*, **190**, 413
- White, D. A., Jones, C., & Forman, W. 1997, *MNRAS*, **292**, 419